

Article

Elucidating Interfacial Hole Extraction and Recombination Kinetics in Perovskite Thin Films

Sunkyu Kim [†], Wonjong Lee [†], Zobia Irshad, Siwon Yun , Hyeji Han, Muhammad Adnan , Hyo Sik Chang 
and Jongchul Lim ^{*} 

Graduate School of Energy Science and Technology, Chungnam National University, Daejeon 34134, Republic of Korea; shinekyu90@gmail.com (S.K.); wjong0227@gmail.com (W.L.); chem.zobia@gmail.com (Z.I.); wlq247@cnu.ac.kr (S.Y.); gpwl0358@gmail.com (H.H.); adnan@cnu.ac.kr (M.A.); hschang@cnu.ac.kr (H.S.C.)

^{*} Correspondence: jclim@cnu.ac.kr

[†] These authors contributed equally to this work.

Abstract: Hybrid organic–inorganic perovskite solar cells (PSCs) are receiving huge attention owing to their marvelous advantages, such as low cost, high efficiency, and superior optoelectronic characteristics. Despite their promising potential, charge-carrier dynamics at the interfaces are still ambiguous, causing carrier recombination and hindering carrier transport, thus lowering the open-circuit voltages (V_{oc}) of PSCs. To unveil this ambiguous phenomenon, we intensively performed various optoelectronic measurements to investigate the impact of interfacial charge-carrier dynamics of PSCs under various light intensities. This is because the charge density can exhibit different mobility and charge transport properties depending on the characteristics of the charge transport layers. We explored the influence of the hole transport layer (HTL) by investigating charge transport properties using photoluminescence (PL) and time-resolved (TRPL) to unveil interfacial recombination phenomena and optoelectronic characteristics. We specifically investigated the impact of various thicknesses of HTLs, such as 2,2',7,7'-tetrakis[*N,N*-di(4-methoxyphenyl)amino]-9,9'-spirobifluorene (spiro-OMeTAD), and poly(triaryl)amine (PTAA), on $\text{FA}_{0.83}\text{MA}_{0.17}\text{Pb}(\text{Br}_{0.05}\text{I}_{0.95})_3$ perovskite films. The HTLs are coated on perovskite film by altering the HTL's concentration and using F4-TCNQ and 4-*tert*-butylpyridine (*t*BP) and lithium bis(trifluoromethanesulfonyl)imide (LiTFSi) as dopants both for spiro-OMeTAD and PTAA. These HTLs diversified the charge concentration gradients in the absorption layer, thus leading to different recombination rates based on the employed laser intensities. At the same time, the generated charge carriers are rapidly transferred to the interface of the HTL/absorption layer and accumulate holes at the interface because of inefficient capacitance and mobility differences caused by differently doped HTL thicknesses. Notably, the charge concentration gradient is low at lower light intensities and did not accumulate holes at the HTL/absorption layer interface, even though they have high charge mobility. Therefore, this study highlights the importance of interfacial charge recombination and charge transport phenomena to achieve highly efficient and stable PSCs.

Keywords: optoelectronic analysis; interfacial charge extraction; perovskite; hole transport layer



Citation: Kim, S.; Lee, W.; Irshad, Z.; Yun, S.; Han, H.; Adnan, M.; Chang, H.S.; Lim, J. Elucidating Interfacial Hole Extraction and Recombination Kinetics in Perovskite Thin Films. *Energies* **2024**, *17*, 2062. <https://doi.org/10.3390/en17092062>

Academic Editor: Robert A. Varin

Received: 20 March 2024

Revised: 16 April 2024

Accepted: 25 April 2024

Published: 26 April 2024



Copyright: © 2024 by the authors. Licensee MDPI, Basel, Switzerland. This article is an open access article distributed under the terms and conditions of the Creative Commons Attribution (CC BY) license (<https://creativecommons.org/licenses/by/4.0/>).

1. Introduction

Recent advances have increased the efficiency of perovskite solar cells (PSCs) to a peak value of 26.1% [1]. This is a significant improvement from the initial efficiency of 3.9% [2], raising the possibility of next-generation solar cells. To enhance photovoltaic efficiency, exciton binding energy is an important factor for the light harvesting materials such as the perovskite semiconductor. Reducing the exciton binding energy can increase the concentration of free electrons and holes within the perovskite layer. To achieve that, there are various approaches, for instance, employing a functional moiety for induced dipole moments [3,4], utilization of high dielectric constant materials [5,6], and optical reflection layers, especially

for utilizing plasmonic effects [7–9]. Recombination between electrons and holes that occurs at the interface between the absorption layer and the HTL becomes a major issue. The electrons and holes at the interface between the absorption layer and the HTL are major issues that cause the efficiency decrease due to a decrease in open-circuit voltage (V_{oc}). Research is being conducted to analyze the charge transport that occurs between the HTL and the absorption layer by changing the HTL conditions. HTL is responsible for transporting holes from the absorption layer to the electrode [10,11]. A major significant advantage of organic HTL is that many properties can be imparted by changing the length of the main chain or functional groups [12–16]. For this work, we used $\text{FA}_{0.83}\text{MA}_{0.17}\text{Pb}(\text{Br}_{0.05}\text{I}_{0.95})_3$ composition, and according to the reported literature, respective exciton binding energy is commonly known to be approximately 7~8 meV [17]. Both the reduction in exciton binding energy and the low recombination rates can increase charge carrier density and improve interfacial injection. While acknowledging the crucial role of exciton binding energy in perovskite, our study focused on varying the internal charge carrier density via excitation density control (laser intensity) rather than using various methods of altering exciton binding energy, as mentioned above. Here, we explored the effect of charge carrier density on the charge transfer at the perovskite/HTL interface. Especially, we aimed to investigate the role of HTLs' optoelectronic properties at the interface while the optoelectronic properties of the perovskite film were controlled to be consistent. Therefore, we selected two HTLs (showing different charge carrier dynamics) and investigated the correlation between thickness, doping control, and, consequently, the charge carrier density-dependent transport. In conventional n-i-p-structured solar cells, spiro-OMeTAD is a widely used HTL for achieving high efficiency [18–20]. Poly[bis(4-phenyl)(2,4,6-trimethylphenyl)amine] (PTAA) is also widely utilized HTL due to its high hydrophobicity and robust long-term stability, which has been a subject of extensive research [21–23]. Additionally, dopant incorporation offers the advantage of enhancing mobility and increasing the capacitance of HTL [24–26]. Although these dopants are frequently used to obtain high efficiency, their penetration promotes moisture absorption, thereby compromising long-term stability [27–29]. To compensate for these degradations, many studies have been conducted on a dopant-free HTL [30–36]. To understand the impact of dopants on HTL, among various optoelectronic analyses, (time-resolved) photoluminescence (PL and TRPL) is a widely used method to measure the charge carrier lifetime. The principle behind these optoelectronic measurements involves illuminating the light onto the sample and measuring the emitted light during the recombination of electrons and holes. Exciton dissociation efficiency and recombination rate are essential to improve photovoltaic efficiency. The perovskite solar cells achieve a good exciton dissociation due to their low exciton binding energy [37,38]. Therefore, we considered the exciton dissociation efficiency as the minor factor and focused on the change in the recombination rate. The amounts of charge carriers change depending on the amount of light irradiated. PL is a quantitative analysis method that measures light intensity at various wavelengths emitted from a sample when electrons and holes recombine within the sample. Similarly, TRPL is a kinetic-based analytical method that predicts the movement of electrons and holes in the sample by measuring the emitted light when electrons and holes are separate and recombined over time. As the charge separates and moves into the CTL, the charge concentration gradient within the perovskite differs, leading to diverse recombination rates. Researchers commonly use optoelectronic analysis to investigate sample properties [39–41]. Therefore, we comprehensively investigated the behavior of charge carriers using optoelectronic analysis. As a result, the amount of charge carriers changes due to the difference in illuminated light. These measurements allowed us to observe a broader range of phenomena. We adjusted the film thickness and dopant concentration. Additionally, we performed measurements under various conditions to observe the internal charge density (Figure 1). As depicted in Figure 1, the influence of doping facilities on energy level alignment. This results in reduced recombination of carriers at the interface, assisting their migration toward the HTL layer [42,43]. Additionally, it also influences the mobility of internal charges, thereby resulting in improved efficiency

of PSCs [44]. We investigated the correlation between the emitted PL intensity and the incident carrier characteristics depending on the number of excitons transferred. Therefore, these results will create a better understanding of the charge carrier properties and can facilitate the optimization of HTL materials.

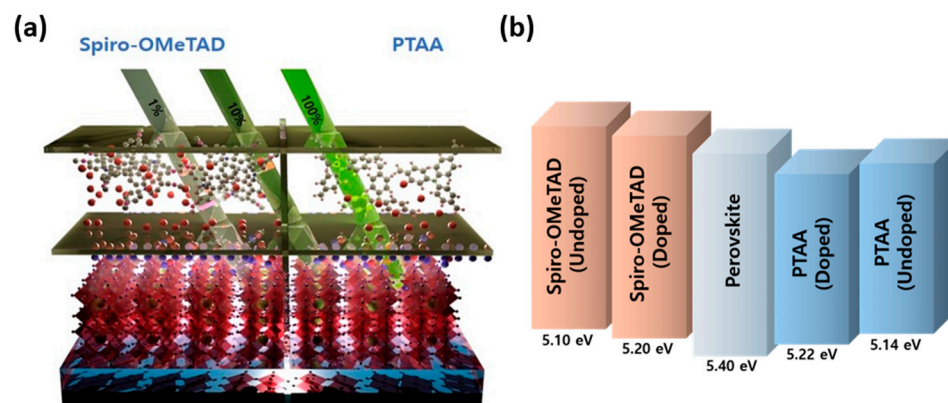


Figure 1. (a) Schematic diagram of experimental method. (b) Energy band diagram of spiro-OMeTAD and PTAA.

2. Materials and Methods

2.1. Materials

Formamidinium iodide (FAI, 99.99%), Methylammonium bromide (MABr, 99.99%), and Methylammonium chloride (MACl, 99.99%) were purchased from GreatCell Solar, Queanbeyan, NSW, Australia. Lead (II) bromide (PbBr_2 , 99.999%) and 2,2',7,7'-Tetrakis[*N,N*-di(4-methoxyphenyl)amino]-9,9'-spirobifluorene (spiro-OMeTAD, 1225.43 g/mol) were purchased from Lumtec, New Taipei City, Taiwan. Poly(triaryl amine), Poly[bis(4-phenyl)(2,4,6-trimethylphenyl)amine] (PTAA, M_n 7000–10,000), and 2,3,5,6-Tetrafluoro-7,7,8,8-tetracyanoquinodimethane (F4-TCNQ, 99%) were purchased from Ossila, Sheffield, UK. Lead(II) iodide (PbI_2 , 99.99%) and lithium Bis(trifluoromethanesulfonyl)imide (LiTFSi, 98%) were purchased from TCI, Tokyo, Japan. Chlorobenzene (CB, 99.7%), Dimethylformamide (DMF, 99%), Dimethyl sulfoxide (DMSO, 99%), and 4-*tert*-Butylpyridine (*t*BP, M_w 135.21) were purchased from Sigma-Aldrich, St. Louis, MO, USA.

Perovskite precursor solution: the $\text{FA}_{0.83}\text{MA}_{0.17}\text{Pb}(\text{I}_{0.83}\text{Br}_{0.17})_3$ perovskite films were deposited from a precursor solution containing FAI (32.61 mg), PbI_2 (87.45 mg), MABr (1.05 mg), PbBr_2 (3.55 mg), and MACl (4.5 mg) in anhydrous DMF (1.2 mL) DMSO (0.15 mL).

2.2. Device Fabrication

The ITO glasses were washed in order with detergent, acetone, ethanol, and deionized water, then ultrasonic-cleaned with detergent and deionized water, acetone, and ethanol for 15 min. After drying in the oven with N_2 , ITO glasses were treated with UV-ozone for 30 min. Then, the SnO_2 solution was spin-coated onto the ITO substrates at 3000 rpm for 30 s; then, the samples were heated on a hotplate at 150 °C for 30 min. The perovskite precursor solution was spin-coated on the SnO_2 -coated ITO substrates at 3000 rpm for 30 s, and 150 μL ethyl acetate was used as the anti-solvent at 8 s. After that, samples were immediately annealed on a hotplate at 150 °C for 15 min in an N_2 filled glovebox. Hole transport material, PTAA solution (14 mg/mL in CB), and spiro-OMeTAD (72.50 mg/mL in CB) were used for HTL precursor and were diluted in CB (100, 50, 33%). They were spin-coated at the top of the perovskite layer at 2000 rpm for 30 s. Finally, Au electrodes (45 nm) were deposited by thermal evaporation under a pressure of 3×10^{-6} torr.

2.3. Doping Methods

Spiro-OMeTAD was doped with LiTFSi (8.75 μL), *t*BP (13.75 μL), and F4-TCNQ (1 wt%) was used for dopant PTAA was doped with LiTFSi (1.715 μL), *t*BP (2.8 μL), and F4-TCNQ (1 wt%).

2.4. Measurements and Characterization

Photoluminescence (PL) and time-resolved photoluminescence (TRPL) spectroscopy used a time-correlated single-photon counting module (TCSPC FluoTime 300 by picoquant, GmbH). The PL measured a 10 MHz frequency, 0.0125 uJ/cm^2 /pulse energy density, and the TRPL measured a 0.2 MHz frequency and 0.011 uJ/cm^2 /pulse.

The J-V traces were measured using a computer-controlled 2450 Series Keithley source meter in the dark under room temperature and humidity. The P-type structure behaved as a Glass/Au/PTAA/PFN-Br/perovskite/HTL/Au configuration.

The PTAA solution for the bottom hole transport layer was prepared by dissolving 2 mg of PTAA in 1 mL of toluene. We spin-coated at 4500 rpm for 30 s. The PFN-Br was prepared by dissolving 1.5 mg in 1 mL of Methanol and spin-coated at 5000 rpm for 30 s.

Electrochemical impedance spectroscopy (EIS) measurements were performed under dark room conditions using an Autolab 302 N at a DC bias potential of 1.0 V and from 10 mHz to 1 MHz. The plots were then fitted using the ThalesXT 5.8.3. The scanning electron microscopy (SEM) images were taken using Merlin Compact, Carl Zeiss (Oberkochen, Germany) microscopes with SmartSEM 5.09 (beam accelerator voltages: 3 keV for cross-sectional images and 3 or 5 kV was used to obtain the surface and cross-sectional morphology views of the perovskite films for the surface morphology). The absorption spectra for the perovskite films prepared on glass/perovskite/HTL layers were measured by UV-vis spectrophotometer UV-red-PMT monochromator (MSH300PQ-0002, picoquant). The J-V measurement was performed under an irradiation intensity of 100 mW cm^{-2} by Ivium Stat MUM technologies under an Am 1.5 solar stimulator.

3. Results and Discussions

Perovskite thin films were prepared with $\text{FA}_{0.83}\text{MA}_{0.17}\text{Pb}(\text{Br}_{0.05}\text{I}_{0.95})_3$ composition using the anti-solvent method. Spiro-OMeTAD and PTAA were used as HTL, and their thicknesses were varied by varying the solution concentration (100, 50, 33%). Subsequently, doping was performed using F4-TCNQ and 4-tert-butylpyridine (*t*BP) and lithium bis(trifluoromethanesulfonyl)imide (LiTFSi). We altered the condition of HTL, maintaining the same conditions of the absorption layer. The HTL layer thickness was measured using a scanning electron microscope (SEM) provided in Figure A1. Subsequently, optoelectronic measurements were performed. PL measurements provide quantitative data. It is advantageous when comparing charge carrier concentration in samples where hole extraction in the HTL reduces recombination. PL measurements were performed using a 520 nm diode laser LDH-P-C-520 at five laser intensity conditions (1, 5, 10, 50, 100%) because the samples had similar absorption spectra at 520 nm (Figure A2), and it was modulated using an OD filter. The remarkable data were obtained during the measurements (Figure 2). While doping spiro-OMeTAD with data points of more than 10%, the PL intensity reversal phenomenon was observed. This suggests that variations in internal carrier density can affect measurements. Indeed, no PL intensity reversal phenomenon was observed in the pure spiro-OMeTAD film, as shown in Figure 2a–c. On the contrary, when PTAA was used as HTL, no reversal phenomenon of PL intensity was observed in PL measurements even after doping, as we see in Figure 2d–f. In other words, the characteristics of HTL can be measured by changing the internal charge density via PL measurements. Subsequently, we experimented to observe if this phenomenon could occur for two reasons. First, when we measured samples using PTAA as HTL when samples were exposed to even 100% laser intensity, PL intensity showed a consistent pattern across different dopant concentrations and thicknesses. Therefore, it can be inferred that observed differences in PL measurements are due to differences in the material properties between spiro-OMeTAD and PTAA. PL

phenomenon of undoped spiro-OMeTAD remained consistent regardless of changes in the carrier concentration. On the other hand, doped spiro-OMeTAD exhibited a clear trend. Based on this data, we hypothesized that this phenomenon in the spiro-OMeTAD sample results from changes in the internal charge carrier density influenced by the presence of the dopants, which led us to proceed with subsequent experiments. TRPL measurements were performed for each sample to evaluate the extraction rate from the absorption layer to HTL. The tri-exponential equation was used for fitting [45,46]. We assumed three mechanisms underlying electron recombination. The fastest decay is attributed to recombination resulting from rapid trapping; the second decay results from recombination at the interface between the absorption layer and HTL, and the last recombination pathway occurs within the bulk perovskite layer [47].

$$A_1 \exp\left[-\left(\frac{t}{\tau_1}\right)\right] + A_2 \exp\left[-\left(\frac{t}{\tau_2}\right)\right] + A_3 \exp\left[-\left(\frac{t}{\tau_3}\right)\right] \quad (1)$$

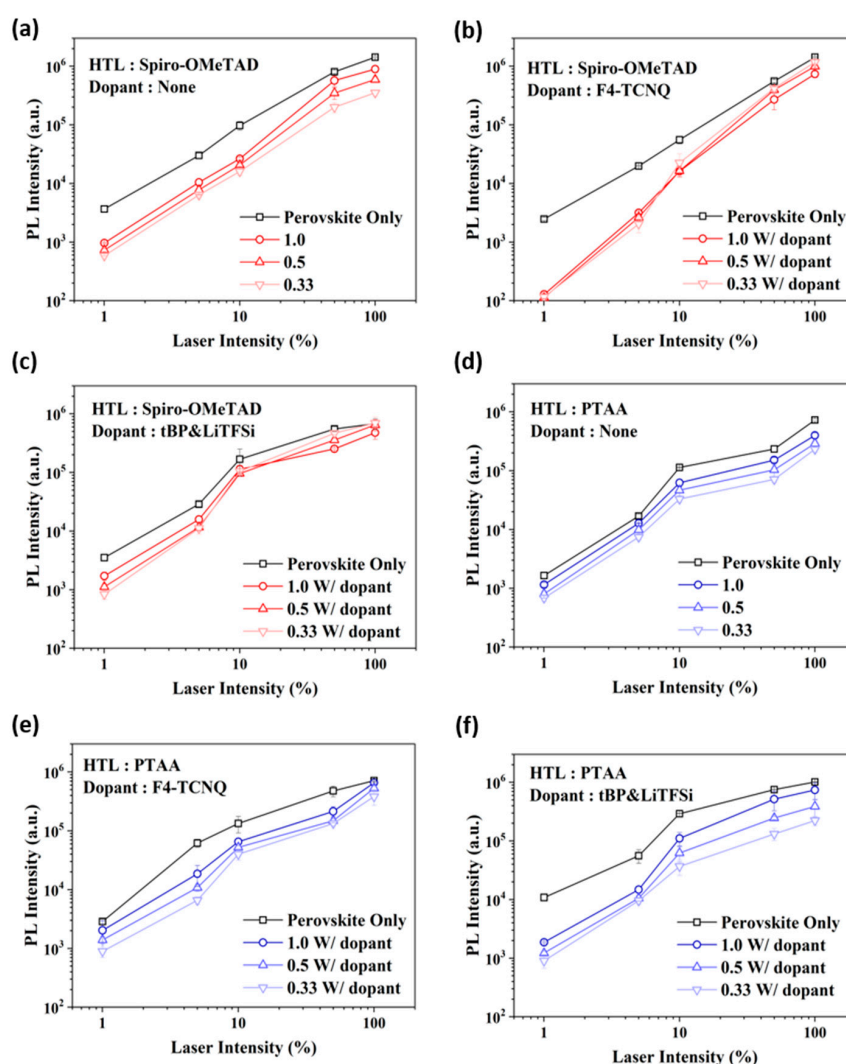


Figure 2. PL measurement results according to different conditions of HTL. The 1.0, 0.5, 0.33 mean precursor concentrations of HTL to change thickness. (a–c) PL intensity measurement of Glass/Perovskite/spiro-OMeTAD. (a) W/O dopant. (b) Using *t*BP and LiTFSi as dopants. (c) Using F4-TCNQ as a dopant. (d–f) PL intensity measurement Glass/Perovskite/PTAA structure. (d) W/O dopant. (e) Using *t*BP and LiTFSi as dopants. (f) Using F4-TCNQ as a dopant. Spiro-OMeTAD with dopant shows noticeable changes when laser intensity increases. On the contrary, samples with PTAA show a constant tendency regardless of laser intensity.

In this equation, ‘ A ’ represents the amplitude of each value, and ‘ τ ’ represents the calculated decay. ‘ τ_1 ’, which exhibits the fastest decay, is denoted as rapid recombination, where electrons rapidly recombine with holes due to the trap state. ‘ τ_2 ’ corresponds to the decay observed during charge extraction from the perovskite to HTL, and ‘ τ_3 ’ refers to the decay interpreted as PL caused by a recombination phenomenon occurring within the bulk perovskite. Figure 3 represents data of the ‘ τ_2 ’ values, which allow us to compare the charge extraction rates between all samples based on laser intensity. When we check Figure 3a,b, doped spiro-OMeTAD, *t*BP, LiTFSi, and F4-TCNQ exhibited faster charge extraction rates across all light intensities. When we check Figure 3a,b, doped spiro-OMeTAD, *t*BP, LiTFSi, and F4-TCNQ exhibited faster charge extraction rates across all light intensities. Consequently, when PTAA was used as HTL, no reversal of PL intensity was observed. This reversal phenomenon can be interpreted as being caused by the change in properties by doping spiro-OMeTAD. Space-charge limited current (SCLC) measurements were performed to evaluate the unique properties due to doping. This is a suitable method to assess the impact of HTL on reaction rates within the sample. SCLC measurements were performed on hole-only structures utilizing a dark-state measurement configuration (Au/PTAA/PFN:Br/Perovskite/HTL/Au). Pulsed voltage measurements are used to minimize hysteresis. Child’s law was applied in the $n = 1$ region during SCLC measurements to determine the conductivity [48].

$$J = \sigma E = en \frac{V}{L} \quad (2)$$

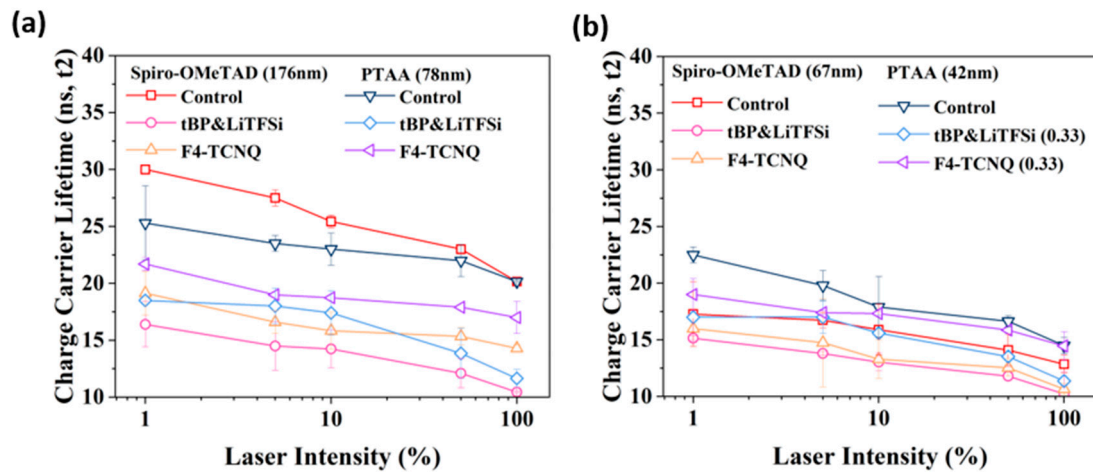


Figure 3. TRPL results of the sample structure with Glass/Perovskite/HTL. The intensity of the irradiated light was 1%, 5%, 10%, 50%, and 100%, the intensity of the light source was changed using an OD filter. During the measurement, the light irradiated at the direction of the film. The τ -value was calculated using the tri-exponential function. Only τ_2 -value was compared as an indicator that can compare the hole extraction velocity of HTL. (a) Comparison of conditions with a solution concentration of 1.0. (b) Comparison of conditions with a solution concentration of 0.33. The line is not a measured point; it is only for guidance.

Here, ‘ E ’ is the electron charge ($=V/L$); ‘ σ ’ represents the charge density; ‘ V ’ denotes the applied voltage, and ‘ L ’ is the thickness of the device. Additionally, the values in the $n = 2$ region can be calculated using Mott–Gurney’s law to determine the mobility.

$$J = \frac{9}{8} \epsilon_r \epsilon_0 \frac{V^2}{L^3} \quad (3)$$

‘ J ’ represents charge density; ‘ ϵ_r ’ denotes dielectric constant; ‘ ϵ_0 ’ is permittivity in free space; ‘ μ ’ denotes mobility; ‘ V ’ represents voltage, and ‘ L ’ is the thickness of the active

layer. SCLC measurements allowed us to compare mobility and conductivity values. The results indicate that the trends in mobility and conductivity values are different depending on the type of HTL. First, when we compare the hole mobility values within perovskite (Figure 4a), it is clear that spiro-OMeTAD exhibits higher mobility than PTAA when using the same dopants. Comparing F4-TCNQ and *t*BP and LiTFSi as dopants, the results show that mobility is faster when F4-TCNQ is used as a dopant in both HTLs (Figure 4). On the contrary, when comparing the conductivity values, it is clear that PTAA exhibits higher conductivity than spiro-OMeTAD. The expression for calculating conductivity can be expressed as follows.

$$\sigma = e(nn + pp) \quad (4)$$

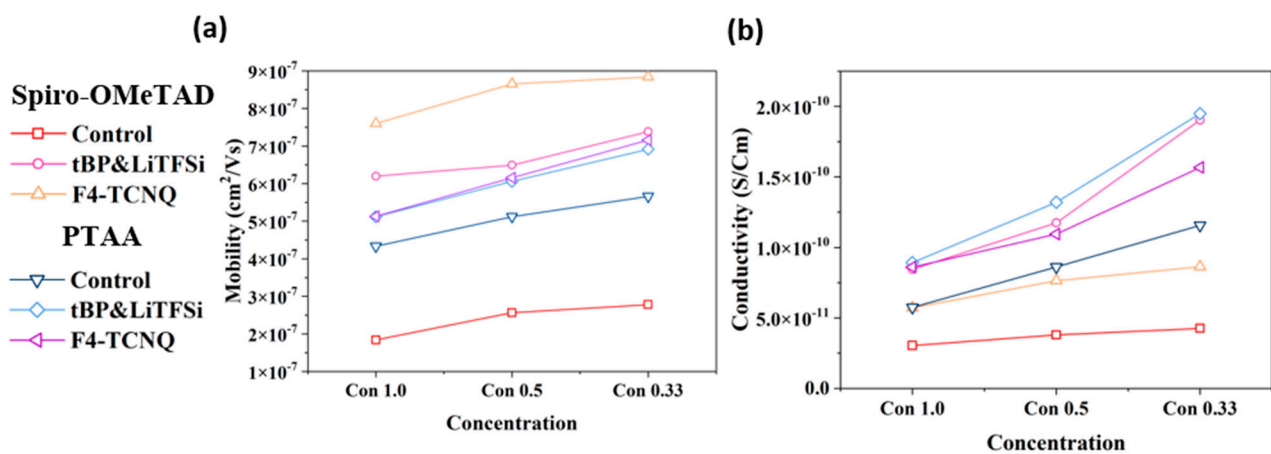


Figure 4. SCLC measurement values. Concentration refers to changes made to control the thickness of the films. (a) Mobility values of each condition. (b) Conductivity value of the samples with different HTL and doping material. SCLC measurements have been performed for both forward and reverse measurements, and hysteresis is less than 1%.

In this equation, '*e*' represents the elementary charge; '*n*' and '*p*' represent the density of electrons and holes in the perovskite layer; ' μ_n ' and ' μ_p ' are the average mobilities of electrons and holes. As a result, electron and hole densities are incorporated into this equation, and their conductivities are calculated. After analyzing the SCLC results, we hypothesize that the initial number of internal ions in the absorption layer remained consistent, but a difference in internal ion density occurred due to the extraction holes promoted by HTL. This discrepancy resulted in higher conductivity values when PTAA was used as the HTL compared to spiro-OMeTAD. Furthermore, when we compare the effects of dopants, F4-TCNQ has lower conductivity than using *t*BP and LiTFSi as dopants, and it also implies that *t*BP and LiTFSi have higher hole capacitances compared to F4-TCNQ. To confirm whether the difference between the mobility and conductivity values arises from the mismatch in the capacitance of the HTL, electrochemical impedance spectroscopy (EIS) measurements were carried out to determine the concentration holes at the interface. We measured the difference in capacitance and resistance caused by accumulation. Measurements were performed in the frequency range of 10 mHz to 1 MHz under dark room conditions. Analyzing the results, we found that different HTL materials had capacitance values. Comparing the effects of dopants while using the same HTL, it is clear that *t*BP and LiTFSi exhibit higher capacitances than F4-TCNQ. Furthermore, spiro-OMeTAD exhibits higher capacitance with increasing concentration due to its thicker HTL (Figure 5). This confirms that the conductivity differences observed in SCLC measurements are due to capacitance differences. Furthermore, regarding the resistance value, if there is not enough space for further movement due to the difference in capacitance, holes are expected to accumulate at the surface, increasing the resistance and reducing the device's efficiency. Therefore, during the PL measurements at laser intensity above 10%, a significant number

of excitons are generated, leading to hole accumulation when the HTL capacity is filled, ultimately causing a decrease in efficiency. The charge carrier dynamics studied in this paper are summarized in Figure A4. The number of free carriers is influenced by the intensity of irradiated light, while the mobility is intrinsic to the type of HTL and is further influenced by the degree of doping. When the number of free carriers with high mobility exceeds the hole capacitance of the HTL, holes accumulate at the perovskite/HTL interface (Figure A4h). In this study, we elucidated the recombination process regarding the hole capacity within the HTL material, resulting in suppressing the recombination phenomena at the perovskite/HTL interfaces. Thereby, the increment of charge carrier density in the device prolonged the lifetime of the holes. Since the recombination phenomena are associated with the hole injection, under a well-aligned energy band, we conducted photovoltaic characterizations and measured PCE of PSC devices fabricated with various HTL thicknesses further to evaluate the impact of HTL thicknesses on the device's performances.

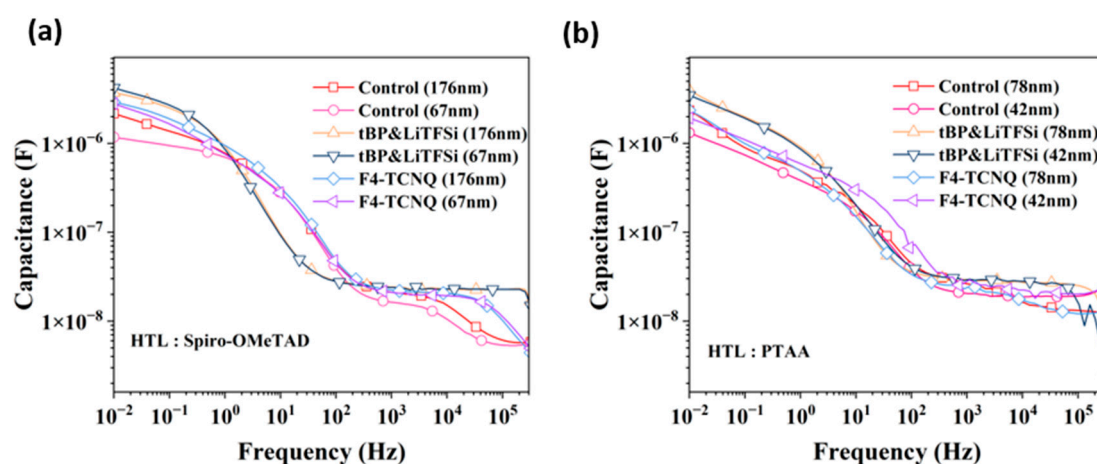


Figure 5. C-F plots of a device with ITO/SnO₂/Perovskite/HTL/Au structure with (a) spiro-OMeTAD; (b) PTAA based on different dopants and thicknesses. Measurements were carried out with the frequency condition set to 10 mHz to 1 MHz under darkroom conditions.

Measurements were conducted under five laser intensity conditions (1, 12.5, 25, 50, 100%) using OD 0.3 and OD 3 filters at an illuminance equivalent to 1 sun and attenuating the light intensity. The device structure was measured in ITO/SnO₂/Perovskite/HTL/Au, which is an n-i-p conventional structure. First, using spiro-OMeTAD doped with F4-TCNQ, *t*BP, and LiTFSi, an efficiency reversal phenomenon is observed at around 10% light intensity compared to PL measurements.

The results can be interpreted as under low light conditions (<12.5%); low concentrations of HTL exhibit high PCE. This efficiency improvement is due to the high mobility and low capacitance confirmed in the previous measurements, and the high efficiency is obtained due to the low concentration of generated charge carriers. Furthermore, at lower light density, no accumulation of holes at the interface occurs due to the lower density of free carriers generated, resulting in faster mobility and sufficient capacitance. However, due to the relative lack of HTL capacitance during measurements, a reversal phenomenon occurred at intensities above 12.5%. At high intensity (>12.5%), hole accumulation occurs at the interface. High concentrations of spiro-OMeTAD with dopants have relatively low mobility and high capacitance, which explains the high PCE at high light intensities (Figure A3). This can be attributed to the EIS measurement results, showing a relatively higher capacitance than spiro-OMeTAD. The consistent trend observed even under relatively high light intensities can be attributed to this factor. Finally, pure spiro-OMeTAD consistently showed relatively lower mobility in relation to PTAA. This reduction in mobility in the undoped spiro-OMeTAD alleviates charge carrier accumulation at the

interface. Therefore, it is evident that this confirms the consistent trend observed under all light intensities (Figure 6).

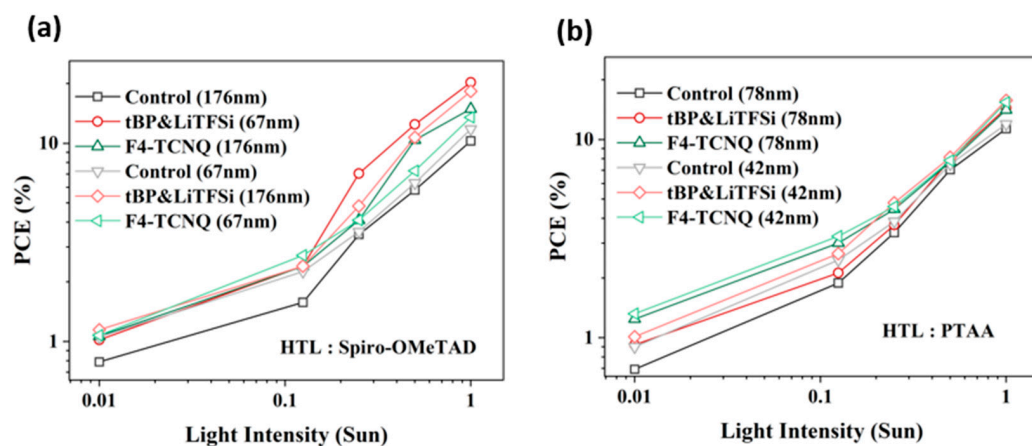


Figure 6. PCE plots of the device with ITO/SnO₂/Perovskite/HTL/Au structure with (a) spiro-OMeTAD and (b) PTAA as HTL. The intensity of the irradiated light placed in the sun (0.01, 0.125, 0.25, 0.5, 1.0) blocks out light by the OD filter.

4. Conclusions

In this study, we comprehensively investigated interface charge recombination and charge transport phenomena when different HTLs were applied to the same absorption layer. When predicting charge transport properties under diverse laser intensity, we find that assessment needs to be carefully interpreted, specifically the presence of different charge carrier gradients. We comprehensively demonstrate our approach, assessing the optoelectronic change via PL and TRPL, charge carrier characteristics via SCLC, interface capacitance characteristics via EIS, and practical performance via PCE. After that, we can obtain an accurate understanding of the overall procedure. Generated charge carrier characteristics are different, in particular, the presence of different HTL and diverse charge concentration gradients leading to different recombination rates at the interfaces. Especially doped spiro-OMeTAD shows remarkable PL tendency. When we irradiate the laser over 10% intensity, thinner HTL shows higher PL intensity than thicker HTL. This effect results from accumulating holes at the interface of the HTL/absorption layer because of insufficient capacitance and rapid transfer of holes due to the high gradient of charge carriers. Conversely, PTAA shows a coherent tendency on PL spectra despite being doped due to relatively lower conductivity and higher capacitance in comparison to spiro-OMeTAD and PTAA due to a low concentration gradient. Overall, we show that interfacial phenomena of the HTL/absorption layer depend on the generated charge concentration gradient. However, the reduction in HTL thickness causes an increase in both mobility and conductivity, accompanied by a decrease in hole capacitance. Consequently, efficiency can be increased when the charge density is low, but when the internal charge density is high, hole extraction kinetics and HTL's capacitance have to be considered to improve the efficiency.

Author Contributions: S.K. conceptualized and designed the overall experiments. S.K. wrote the original draft of the manuscript. W.L. and M.A. provided supervision, writing review, and editing of this work. Z.I. contributed to the discussion and writing of this paper. H.H. and S.Y. participated in formal analysis and data curation. H.S.C. and J.L. provided supervision, sources, funding, writing, and editing. All authors have read and agreed to the published version of the manuscript.

Funding: This work was supported by the National Research Foundation of Korea (NRF) grant funded by the Korean government (MSIT) (No. 2023R1A2C2005172). This work was supported by the Korean Institute of Energy Technology Evaluation and Planning (KETEP) and the Ministry of Trade, Industry, and Energy (MOTIE) of the Republic of Korea (No. RS-2023-00236664).

Data Availability Statement: The data presented in this study are available in the article.

Acknowledgments: We thank the Chungnam National University for providing support for this project.

Conflicts of Interest: There are no conflicts to declare.

Appendix A

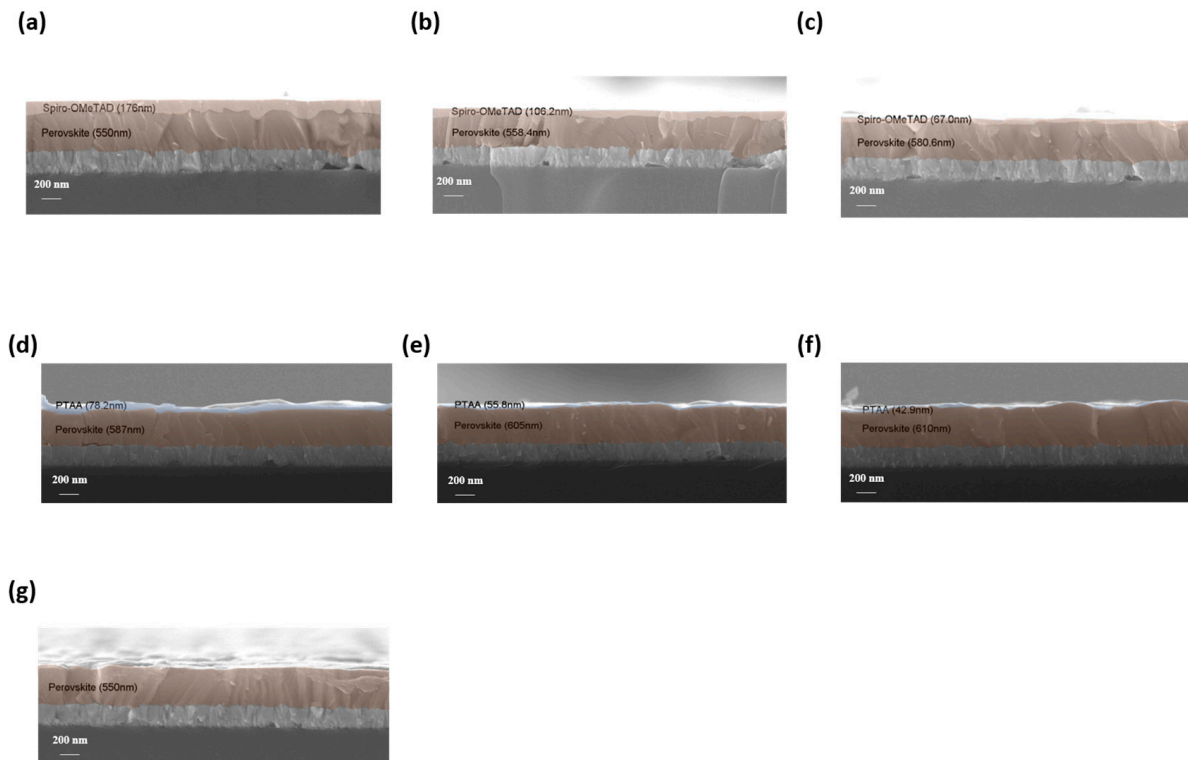


Figure A1. Data from scanning electron microscope (SEM) results to check the change in thickness due to concentration. (a–c) spiro-OMeTAD was used for HTL. (a) The 1.0 concentration of spiro-OMeTAD precursor. (b) 0.5 concentration of spiro-OMeTAD precursor. (c) The 0.33 concentration of spiro-OMeTAD precursor. (d,e) PTAA was used for HTL. (d) The 1.0 concentration of PTAA precursor. (e) The 0.5 concentration of PTAA precursor. (f) The 0.33 concentration of PTAA precursor. (g) Only perovskite layer was measured to ensure thickness.

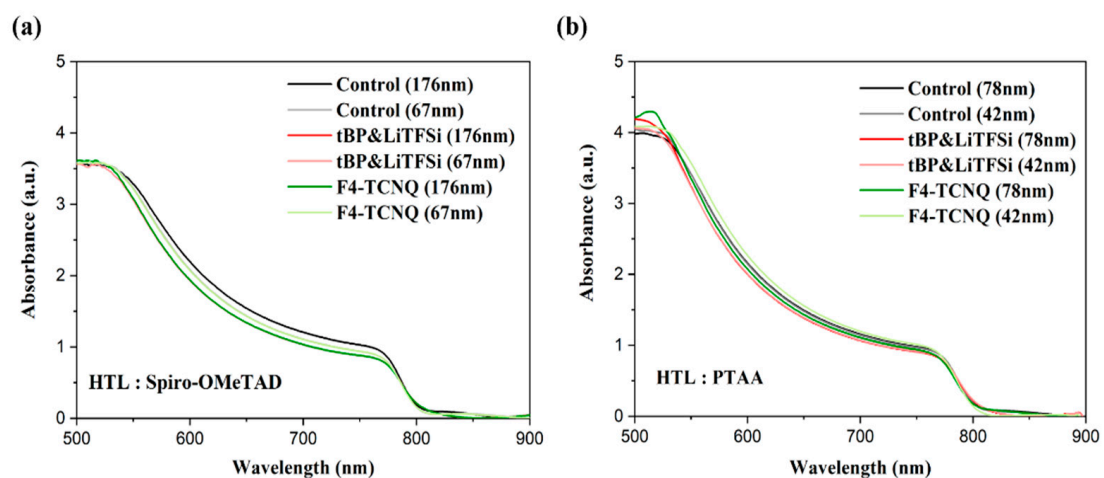


Figure A2. UV-Vis absorption spectra of perovskite thin film. (a) Spiro-OMeTAD (b) PTAA.

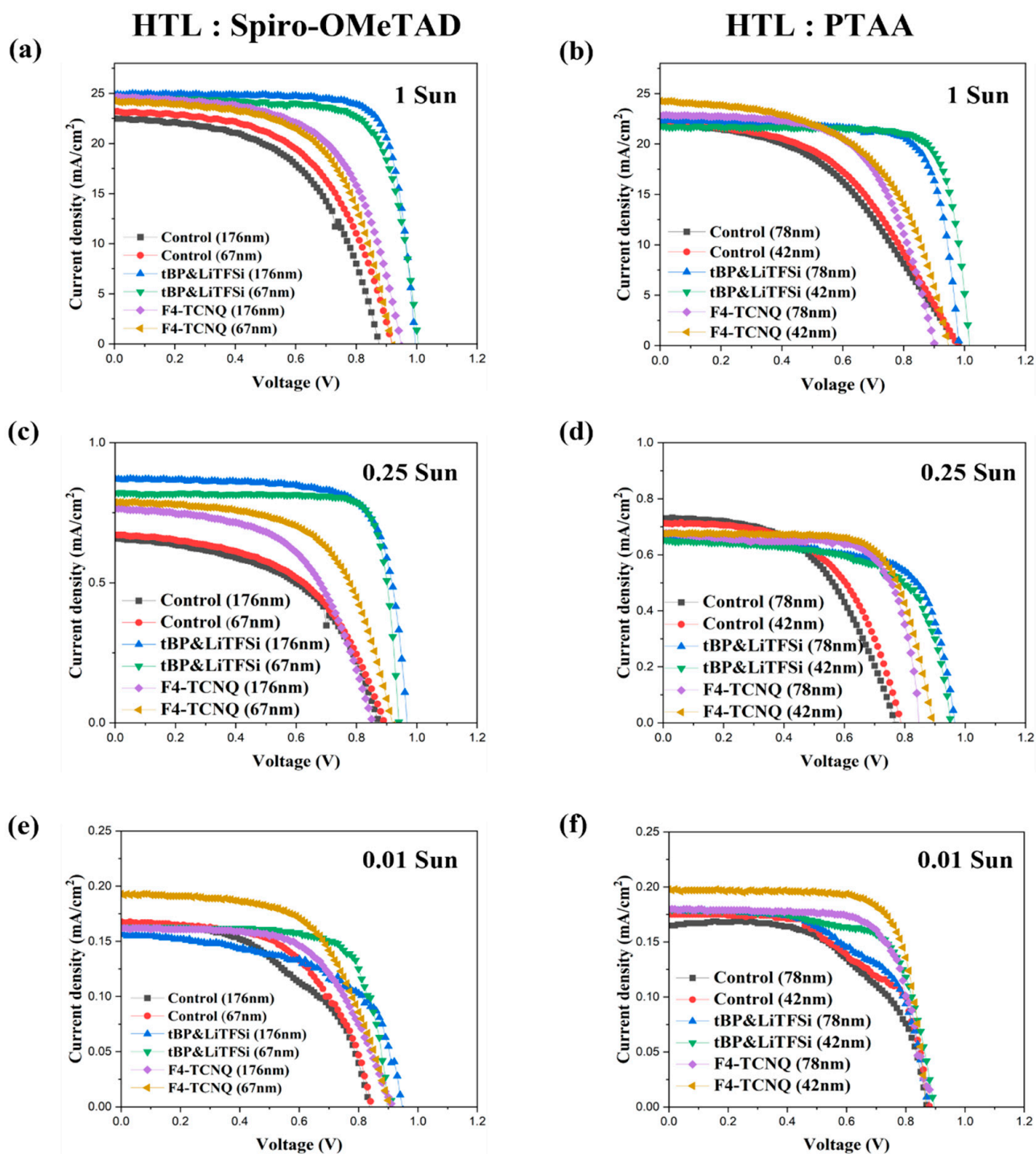


Figure A3. J-V curves according to the sun. (a,c,e) J-V Curve of the Spiro-OMeTAD. (b,d,f) J-V Curve of the PTAA.

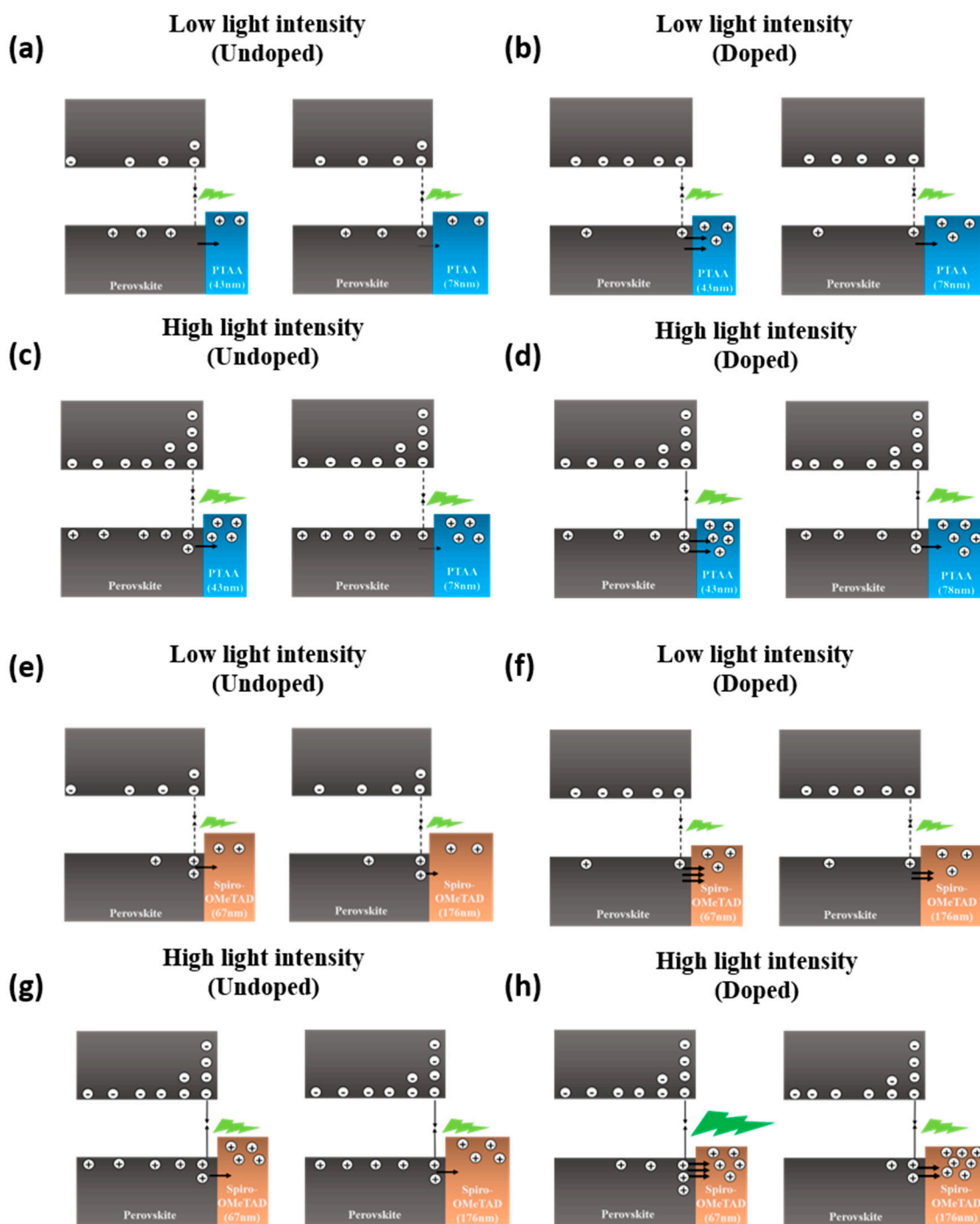


Figure A4. Schematic diagram of the extraction process of charge carriers in a perovskite/PTAA partial device under various conditions. (a) Undoped PTAA with low light intensity. (b) Doped PTAA with low light intensity. (c) Undoped PTAA with high light intensity. (d) Doped PTAA with high light intensity. (e) Undoped Spiro-OMeTAD with low light intensity. (f) Doped Spiro-OMeTAD with high light intensity. (g) Undoped Spiro-OMeTAD with high light intensity. (h) Doped Spiro-OMeTAD with high light intensity.

References

1. Liang, Z.; Zhang, Y.; Xu, H.; Chen, W.; Liu, B.; Zhang, J.; Zhang, H.; Wang, Z.; Kang, D.H.; Zeng, J.; et al. Homogenizing Out-of-Plane Cation Composition in Perovskite Solar Cells. *Nature* **2023**, *624*, 557–563. [[CrossRef](#)] [[PubMed](#)]
2. Raga, S.R.; Jung, M.C.; Lee, M.V.; Leyden, M.R.; Kato, Y.; Qi, Y. Influence of Air Annealing on High Efficiency Planar Structure Perovskite Solar Cells. *Chem. Mater.* **2015**, *27*, 1597–1603. [[CrossRef](#)]

3. Chen, X.; Zheng, S. On the Study of Influence of Molecular Arrangements and Dipole Moment on Exciton Binding Energy in Solid State. *Int. J. Quantum Chem.* **2021**, *121*, 9–13. [[CrossRef](#)]
4. Hamada, M.; Rana, S.; Jokar, E.; Awasthi, K.; Diao, E.W.G.; Ohta, N. Temperature-Dependent Electroabsorption Spectra and Exciton Binding Energy in a Perovskite CH₃NH₃PbI₃Nanocrystalline Film. *ACS Appl. Energy Mater.* **2020**, *3*, 11830–11840. [[CrossRef](#)]
5. Yang, Z.; Surrente, A.; Galkowski, K.; Bruyant, N.; Maude, D.K.; Haghighirad, A.A.; Snaith, H.J.; Plochocka, P.; Nicholas, R.J. Unraveling the Exciton Binding Energy and the Dielectric Constant in Single-Crystal Methylammonium Lead Triiodide Perovskite. *J. Phys. Chem. Lett.* **2017**, *8*, 1851–1855. [[CrossRef](#)] [[PubMed](#)]
6. Kraner, S.; Scholz, R.; Koerner, C.; Leo, K. Design Proposals for Organic Materials Exhibiting a Low Exciton Binding Energy. *J. Phys. Chem. C* **2015**, *119*, 22820–22825. [[CrossRef](#)]
7. Jacak, W.A.; Jacak, J.E. New Channel of Plasmon Photovoltaic Effect in Metalized Perovskite Solar Cells. *J. Phys. Chem. C* **2019**, *123*, 30633–30639. [[CrossRef](#)]
8. Laska, M.; Krzemińska, Z.; Kluczyk-Korch, K.; Schaadt, D.; Popko, E.; Jacak, W.A.; Jacak, J.E. Metallization of Solar Cells, Exciton Channel of Plasmon Photovoltaic Effect in Perovskite Cells. *Nano Energy* **2020**, *75*, 104751. [[CrossRef](#)]
9. Wu, R.; Yang, B.; Zhang, C.; Huang, Y.; Cui, Y.; Liu, P.; Zhou, C.; Hao, Y.; Gao, Y.; Yang, J. Prominent Efficiency Enhancement in Perovskite Solar Cells Employing Silica-Coated Gold Nanorods. *J. Phys. Chem. C* **2016**, *120*, 6996–7004. [[CrossRef](#)]
10. Khan, J.I.; Isikgor, F.H.; Ugur, E.; Raja, W.; Harrison, G.T.; Yengel, E.; Anthopoulos, T.D.; De Wolf, S.; Laquai, F. Charge Carrier Recombination at Perovskite/Hole Transport Layer Interfaces Monitored by Time-Resolved Spectroscopy. *ACS Energy Lett.* **2021**, *6*, 4155–4164. [[CrossRef](#)]
11. Haddad, J.; Krogmeier, B.; Klingebiel, B.; Krückemeier, L.; Melhem, S.; Liu, Z.; Hüpkes, J.; Mathur, S.; Kirchartz, T. Analyzing Interface Recombination in Lead-Halide Perovskite Solar Cells with Organic and Inorganic Hole-Transport Layers. *Adv. Mater. Interfaces* **2020**, *7*, 2000366. [[CrossRef](#)]
12. Pan, Z.; Peng, D.; Zhao, X.; Xu, W.; Bao, Y.; Feng, Z.; Zou, Q.; Xu, B.; Wang, Y.; Gao, H.; et al. Side-Chain Functionalized Polymer Hole-Transporting Materials with Defect Passivation Effect for Highly Efficient Inverted Quasi-2D Perovskite Solar Cells. *Adv. Funct. Mater.* **2023**, *33*, 2304881. [[CrossRef](#)]
13. Al-Ashouri, A.; Köhnen, E.; Li, B.; Magomedov, A.; Hempel, H.; Caprioglio, P.; Márquez, J.A.; Vilches, A.B.M.; Kasparavicius, E.; Smith, J.A.; et al. Monolithic Perovskite/Silicon Tandem Solar Cell with >29% Efficiency by Enhanced Hole Extraction. *Science* **2020**, *370*, 1300–1309. [[CrossRef](#)] [[PubMed](#)]
14. Hoffman, J.B.; Astridge, D.D.; Park, S.Y.; Zhang, F.; Yang, M.; Moore, D.T.; Harvey, S.P.; Zhu, K.; Sellinger, A. Polymer Hole Transport Material Functional Group Tuning for Improved Perovskite Solar Cell Performance. *ACS Appl. Energy Mater.* **2022**, *5*, 8601–8610. [[CrossRef](#)]
15. De Rossi, F.; Renno, G.; Taheri, B.; Yaghoobi Nia, N.; Ilieva, V.; Fin, A.; Di Carlo, A.; Bonomo, M.; Barolo, C.; Brunetti, F. Modified P3HT Materials as Hole Transport Layers for Flexible Perovskite Solar Cells. *J. Power Sources* **2021**, *494*, 229735. [[CrossRef](#)]
16. Xie, Y.; Yao, Q.; Xue, Q.; Zeng, Z.; Niu, T.; Zhou, Y.; Zhuo, M.; Tsang, S.; Yip, H.; Cao, Y. Subtle Side Chain Modification of Triphenylamine-based Polymer Hole-transport Layer Materials Produces Efficient and Stable Inverted Perovskite Solar Cells. *Interdiscip. Mater.* **2022**, *1*, 281–293. [[CrossRef](#)]
17. Ali, R.; Zhu, Z.G.; Yan, Q.B.; Zheng, Q.R.; Su, G.; Laref, A.; Saraj, C.S.; Guo, C. Compositional Engineering Study of Lead-Free Hybrid Perovskites for Solar Cell Applications. *ACS Appl. Mater. Interfaces* **2020**, *12*, 49636–49647. [[CrossRef](#)] [[PubMed](#)]
18. Ouedraogo, N.A.N.; Odunmbaku, G.O.; Guo, B.; Chen, S.; Lin, X.; Shumilova, T.; Sun, K. Oxidation of Spiro-OMeTAD in High-Efficiency Perovskite Solar Cells. *ACS Appl. Mater. Interfaces* **2022**, *14*, 34303–34327. [[CrossRef](#)] [[PubMed](#)]
19. Chen, Q.; Wu, J.; Wang, X.; Yang, Y.; Du, Y.; Li, Z.; Zhang, X.; Zhang, Z.; Pan, W.; Sun, W. Spiro-OMeTAD Doped with Cumene Hydroperoxide for Perovskite Solar Cells. *Electrochem. Commun.* **2021**, *126*, 107020. [[CrossRef](#)]
20. Arivunithi, V.M.; Park, H.Y.; Reddy, S.S.; Do, Y.; Park, H.; Shin, E.S.; Noh, Y.Y.; Song, M.; Jin, S.H. Introducing an Organic Hole Transporting Material as a Bilayer to Improve the Efficiency and Stability of Perovskite Solar Cells. *Macromol. Res.* **2021**, *29*, 149–156. [[CrossRef](#)]
21. Li, Y.; Wang, B.; Liu, T.; Zeng, Q.; Cao, D.; Pan, H.; Xing, G. Interfacial Engineering of PTAA/Perovskites for Improved Crystallinity and Hole Extraction in Inverted Perovskite Solar Cells. *ACS Appl. Mater. Interfaces* **2022**, *14*, 3284–3292. [[CrossRef](#)] [[PubMed](#)]
22. Zhao, X.; Wang, M. Organic Hole-Transporting Materials for Efficient Perovskite Solar Cells. *Mater. Today Energy* **2018**, *7*, 208–220. [[CrossRef](#)]
23. He, M.; Chen, S.; Wang, T.; Xu, G.; Liu, N.; Xu, F. Effects of Solvent Vapor Atmosphere on Photovoltaic Performance of Perovskite Solar Cells. *Crystals* **2023**, *13*, 549. [[CrossRef](#)]
24. Wang, Q.; Bi, C.; Huang, J. Doped Hole Transport Layer for Efficiency Enhancement in Planar Heterojunction Organolead Trihalide Perovskite Solar Cells. *Nano Energy* **2015**, *15*, 275–280. [[CrossRef](#)]
25. Seo, J.Y.; Akin, S.; Zalibera, M.; Preciado, M.A.R.; Kim, H.S.; Zakeeruddin, S.M.; Milić, J.V.; Grätzel, M. Dopant Engineering for Spiro-OMeTAD Hole-Transporting Materials towards Efficient Perovskite Solar Cells. *Adv. Funct. Mater.* **2021**, *31*, 2102124. [[CrossRef](#)]
26. Wang, C.; Su, Z.; Chen, L.; Zhang, H.; Hui, W.; Liang, D.; Zheng, G.; Zhang, L.; Tang, Z.; Wen, W.; et al. MoO₃ Doped PTAA for High-Performance Inverted Perovskite Solar Cells. *Appl. Surf. Sci.* **2022**, *571*, 151301. [[CrossRef](#)]

27. Matsushita, A.; Yanagida, M.; Shirai, Y.; Miyano, K. Degradation of Perovskite Solar Cells by the Doping Level Decrease of HTL Revealed by Capacitance Spectroscopy. *Sol. Energy Mater. Sol. Cells* **2021**, *220*, 110854. [[CrossRef](#)]
28. Wang, S.; Huang, Z.; Wang, X.; Li, Y.; Günther, M.; Valenzuela, S.; Parikh, P.; Cabrerros, A.; Xiong, W.; Meng, Y.S. Unveiling the Role of TBP-LiTFSI Complexes in Perovskite Solar Cells. *J. Am. Chem. Soc.* **2018**, *140*, 16720–16730. [[CrossRef](#)]
29. Hatamvand, M.; Vivo, P.; Liu, M.; Tayyab, M.; Dastan, D.; Cai, X.; Chen, M.; Zhan, Y.; Chen, Y.; Huang, W. The Role of Different Dopants of Spiro-OMeTAD Hole Transport Material on the Stability of Perovskite Solar Cells: A Mini Review. *Vacuum* **2023**, *214*, 112076. [[CrossRef](#)]
30. Wang, R.T.; Zhang, Y.; Wu, X.; Zhang, W.; Chi, L.; Xu, F. Stable FAPbI₃ Hydrate Structure by Kinetics Negotiation for Solar Cells. *Sustain. Energy Fuels* **2023**, *7*, 1974–1980. [[CrossRef](#)]
31. Zhang, Z.; Fu, J.; Chen, Q.; Zhang, J.; Huang, Z.; Cao, J.; Ji, W.; Zhang, L.; Wang, A.; Zhou, Y.; et al. Dopant-Free Polymer Hole Transport Materials for Highly Stable and Efficient CsPbI₃ Perovskite Solar Cells. *Small* **2023**, *19*, 2206952. [[CrossRef](#)] [[PubMed](#)]
32. Más-Montoya, M.; Gómez, P.; Wang, J.; Janssen, R.A.J.; Curiel, D. Small Molecule Dopant-Free Dual Hole Transporting Material for Conventional and Inverted Perovskite Solar Cells. *Mater. Chem. Front.* **2023**, *7*, 4019–4028. [[CrossRef](#)]
33. Luo, W.; Wu, C.; Wang, D.; Zhang, Z.; Qi, X.; Guo, X.; Qu, B.; Xiao, L.; Chen, Z. Dopant-Free Spiro-OMeTAD as Hole Transporting Layer for Stable and Efficient Perovskite Solar Cells. *Org. Electron.* **2019**, *74*, 7–12. [[CrossRef](#)]
34. Cheng, Q.; Chen, H.; Chen, W.; Ding, J.; Chen, Z.; Shen, Y.; Wu, X.; Wu, Y.; Li, Y.; Li, Y. Green Solvent Processable, Asymmetric Dopant-Free Hole Transport Layer Material for Efficient and Stable n-i-p Perovskite Solar Cells and Modules. *Angew. Chem.-Int. Ed.* **2023**, *62*, e202312231. [[CrossRef](#)] [[PubMed](#)]
35. Kim, I.B.; Kim, Y.J.; Kim, D.Y.; Jang, S.Y. A Thiophene Based Dopant-Free Hole-Transport Polymer for Efficient and Stable Perovskite Solar Cells. *Macromol. Res.* **2022**, *30*, 391–396. [[CrossRef](#)]
36. Zhu, H.; Shen, Z.; Pan, L.; Han, J.; Eickemeyer, F.T.; Ren, Y.; Li, X.; Wang, S.; Liu, H.; Dong, X.; et al. Low-Cost Dopant Additive-Free Hole-Transporting Material for a Robust Perovskite Solar Cell with Efficiency Exceeding 21%. *ACS Energy Lett.* **2021**, *6*, 208–215. [[CrossRef](#)]
37. D’Innocenzo, V.; Grancini, G.; Alcocer, M.J.P.; Kandada, A.R.S.; Stranks, S.D.; Lee, M.M.; Lanzani, G.; Snaith, H.J.; Petrozza, A. Excitons versus Free Charges in Organo-Lead Tri-Halide Perovskites. *Nat. Commun.* **2014**, *5*, 3586. [[CrossRef](#)] [[PubMed](#)]
38. Umari, P.; Mosconi, E.; De Angelis, F. Infrared Dielectric Screening Determines the Low Exciton Binding Energy of Metal-Halide Perovskites. *J. Phys. Chem. Lett.* **2018**, *9*, 620–627. [[CrossRef](#)] [[PubMed](#)]
39. van der Pol, T.P.A.; Datta, K.; Wienk, M.M.; Janssen, R.A.J. The Intrinsic Photoluminescence Spectrum of Perovskite Films. *Adv. Opt. Mater.* **2022**, *10*, 2102557. [[CrossRef](#)]
40. Dequillettes, D.W.; Koch, S.; Burke, S.; Paranjji, R.K.; Shropshire, A.J.; Ziffer, M.E.; Ginger, D.S. Photoluminescence Lifetimes Exceeding 8 Ms and Quantum Yields Exceeding 30% in Hybrid Perovskite Thin Films by Ligand Passivation. *ACS Energy Lett.* **2016**, *1*, 438–444. [[CrossRef](#)]
41. Skurlov, I.D.; Yin, W.; Ismagilov, A.O.; Tsytkin, A.N.; Hua, H.; Wang, H.; Zhang, X.; Litvin, A.P.; Zheng, W. Improved One- and Multiple-Photon Excited Photoluminescence from Cd²⁺-Doped CsPbBr₃ Perovskite Ncs. *Nanomaterials* **2022**, *12*, 151. [[CrossRef](#)] [[PubMed](#)]
42. Hawash, Z.; Ono, L.K.; Raga, S.R.; Lee, M.V.; Qi, Y. Air-Exposure Induced Dopant Redistribution and Energy Level Shifts in Spin-Coated Spiro-Meotad Films. *Chem. Mater.* **2015**, *27*, 562–569. [[CrossRef](#)]
43. Tumen-Ulzii, G.; Qin, C.; Matsushima, T.; Leyden, M.R.; Balijipalli, U.; Klotz, D.; Adachi, C. Understanding the Degradation of Spiro-OMeTAD-Based Perovskite Solar Cells at High Temperature. *Sol. RRL* **2020**, *4*, 2000305. [[CrossRef](#)]
44. Luo, J.; Xia, J.; Yang, H.; Chen, L.; Wan, Z.; Han, F.; Malik, H.A.; Zhu, X.; Jia, C. Toward High-Efficiency, Hysteresis-Less, Stable Perovskite Solar Cells: Unusual Doping of a Hole-Transporting Material Using a Fluorine-Containing Hydrophobic Lewis Acid. *Energy Environ. Sci.* **2018**, *11*, 2035–2045. [[CrossRef](#)]
45. Sidhik, S.; Wang, Y.; Li, W.; Zhang, H.; Zhong, X.; Agrawal, A.; Hadar, I.; Spanopoulos, I.; Mishra, A.; Traoré, B.; et al. High-Phase Purity Two-Dimensional Perovskites with 17.3% Efficiency Enabled by Interface Engineering of Hole Transport Layer. *Cell Rep. Phys. Sci.* **2021**, *2*, 100601. [[CrossRef](#)]
46. Peán, E.V.; Dimitrov, S.; De Castro, C.S.; Davies, M.L. Interpreting Time-Resolved Photoluminescence of Perovskite Materials. *Phys. Chem. Chem. Phys.* **2020**, *22*, 28345–28358. [[CrossRef](#)] [[PubMed](#)]
47. Petrović, M.; Maksudov, T.; Panagiotopoulos, A.; Serpetzoglou, E.; Konidakis, I.; Stylianakis, M.M.; Stratakis, E.; Kymakis, E. Limitations of a Polymer-Based Hole Transporting Layer for Application in Planar Inverted Perovskite Solar Cells. *Nanoscale Adv.* **2019**, *1*, 3107–3118. [[CrossRef](#)] [[PubMed](#)]
48. Le Corre, V.M.; Duijnste, E.A.; El Tambouli, O.; Ball, J.M.; Snaith, H.J.; Lim, J.; Koster, L.J.A. Revealing Charge Carrier Mobility and Defect Densities in Metal Halide Perovskites via Space-Charge-Limited Current Measurements. *ACS Energy Lett.* **2021**, *6*, 1087–1094. [[CrossRef](#)] [[PubMed](#)]

Disclaimer/Publisher’s Note: The statements, opinions and data contained in all publications are solely those of the individual author(s) and contributor(s) and not of MDPI and/or the editor(s). MDPI and/or the editor(s) disclaim responsibility for any injury to people or property resulting from any ideas, methods, instructions or products referred to in the content.